

Extending geographically and temporally weighted regression to account for both spatiotemporal heterogeneity and seasonal variations in coastal seas



Zhenhong Du^{a,b,*}, Sensen Wu^a, Feng Zhang^{a,b}, Renyi Liu^{a,b}, Yan Zhou^{c,d}

^a School of Earth Sciences, Zhejiang University, 38 Zheda Road, Hangzhou 310027, China

^b Zhejiang Provincial Key Laboratory of Geographic Information Science, 148 Tianmushan Road, Hangzhou 310028, China

^c Zhejiang Fisheries Tech Extens Ctr, Hangzhou 310013, China

^d Zhejiang Prov Acad Marine Sci, Hangzhou 310012, China

ARTICLE INFO

Keywords:

GcTWR
Spatiotemporal heterogeneity
Seasonal variations
Coastal seas
Chlorophyll-*a*

ABSTRACT

Space-time modelling has been successfully applied in numerous research projects and has been studied extensively in the field of geographical information science. However, the cyclical or seasonal variations in the temporal dimension of most spatiotemporal processes are rarely considered along with spatiotemporal non-stationarity. Seasonal variations are widespread and typical in marine environmental processes, and addressing both spatiotemporal heterogeneity and seasonal variations is particularly difficult in the turbid and optically complex coastal seas. By incorporating seasonal periodic effects into a geographically and temporally weighted regression (GTWR) model, we proposed a geographically and cycle-temporally weighted regression (GcTWR) model. To test its performance, modelling of chlorophyll-*a*, known as an important indicator of the coastal environment, is performed using the in situ data collected from 2012 to 2016 in the coastal sea of Zhejiang Province, China. GcTWR is compared with global ordinary least squares (OLS), geographically weighted regression (GWR), cycle-temporally weighted regression (cTWR), and GTWR models. In the results, the GcTWR model decreases absolute errors by 89.74%, 79.77%, 76.60% and 29.83% relative to the OLS, GWR, cTWR, and GTWR models, and presents a higher R^2 (0.9274) than the GWR (0.5911), cTWR (0.6465), and GTWR (0.8721) models. The estimation results further confirm that the seasonal influences in coastal areas are much more significant than the interannual effects, which accordingly demonstrates that extending the GTWR model to handle both spatiotemporal heterogeneity and seasonal variations are meaningful. In addition, a novel 3D visualization method is proposed to explore the spatiotemporal heterogeneity of the estimation results.

1. Introduction

Space and time are two fundamental dimensions pertaining to all geographic processes. Space-time analysis and modelling of geographic parameters has long been one of the main focuses of geographical information science (GIScience). Examples include investigating the spatiotemporal patterns of real estate prices (Fotheringham et al., 2015; Huang et al., 2010; Lu et al., 2014; Wu et al., 2014), environmental issues (Bai et al., 2016; Chu et al., 2015), land use (Wrenn and Sam, 2014), marine processes (Alam et al., 2016; Terry et al., 2013; Wang et al., 2015) etc. Although the temporal dimension has been incorporated into spatial analysis and modelling successfully in many research projects, cyclical or seasonal variations are rarely managed with spatiotemporal nonstationarity in most geographic processes.

Seasonal variations in marine environmental processes are widespread and typical, and require further exploration and researches (Dango, 2015;

Khodse et al., 2007; Niu et al., 2015). Coastal seas are the richest marine regions in the world, and are the interfacial areas among the marine, terrestrial and aerial environments (Chen and Liu, 2015). Considering the key role of phytoplankton in biogeochemical cycles, phytoplankton biomass in terms of chlorophyll-*a* (Chl-*a*) is considered as the biological indicator of coastal environments and the most important element in coastal ecosystems (Paudel et al., 2016; Su and Weng, 1994). Therefore, investigating the spatiotemporal variations of Chl-*a* and understanding the interactions between Chl-*a* and other environmental factors are of great significance to recognize the ecological state of the coastal areas.

However, the variations of Chl-*a* are difficult to analyse and interpret due to the complicated interrelationships between phytoplankton and marine environmental factors (suspended matter, dissolved oxygen, nutrients, organic solute, etc.). Previous studies have established several global regression models to predict Chl-*a* concentrations. Celik (2006) used a multiple regression model to explore the relations between Chl-*a* and other

* Corresponding author at: School of Earth Sciences, Zhejiang University, 38 Zheda Road, Hangzhou 310027, China.
E-mail address: duzhenhong@zju.edu.cn (Z. Du).

water quality parameters (ammonium (NO₄), nitrate (NO₃) and phosphate (PO₄)). Partial least-squares regression (PLSR) was also employed to address the optimal count of factors that were suitable for estimating Chl-*a*, which was capable to account for 80% of the observed Chl-*a* variations (Ryan and Ali, 2016).

The hypothesis of space-time stationarity in global models is usually impractical since parameters tend to change across the research regions and over time. Therefore, some local models have been put forward to capture spatial variability in marine environmental processes (Freedman and Sen Roy, 2012; Keith et al., 2013). For instance, geographically weighted regression (GWR) model was formulated and fitted by Keith et al. (2013) to investigate the variations in the relations between macroalgae richness and environmental conditions over geographical regions. Furthermore, researches have been conducted to integrate temporal impacts into the GWR model to account for both spatial and temporal heterogeneities in recent years (Crespo, 2009; Fotheringham et al., 2015; Huang et al., 2010). For example, by extending the spatial distance to a spatiotemporal distance, a geographically and temporally weighted regression (GTWR) model was developed by Huang et al. (2010), which has been applied in various fields and has achieved significant performance. In 2015, Fotheringham et al. (2015) also proposed a new GTWR model to deal with local effects in both space and time, which was confirmed to be effective in the modelling of hedonic price.

However, few researches have been carried out on the quantitative effect of marine environmental processes in coastal seas on both spatial and temporal scales. Due to the complex optical and turbid characteristics of coastal regions, managing spatiotemporal nonstationarity in these areas is considerably difficult and challenging. Moreover, studies have shown that seasonal variations are quite significant in the coastal environment. For example, a long period of remote sensing data was used by Chen and Liu (2015) to demonstrate the temporal variations of Chl-*a* and suspended matter, which indicated significantly seasonal changes in the China's eastern coastal zones.

Therefore, to better understand the marine environmental processes in coastal seas, novel approaches should be put forward to deal with the spatiotemporal nonstationarity and seasonal variations simultaneously. By dividing temporal distance into seasonal periodic and interannual aperiodic parts, our study extends the GTWR model of Huang et al. (2010) and proposes a geographically and cycle-temporally weighted regression (GcTWR) model to capture cycle-temporal variations and spatiotemporal heterogeneity. In addition, an innovative 3D visualization method is proposed for presenting the spatiotemporal variations of the estimation results.

Our article is formed as follows. In Section 2, we describe the study area and data. The widely used GWR model is introduced in Section 3, followed up by the process of integrating GTWR with cycle-temporal variations to achieve the GcTWR model. The case study results and discussions of Chl-*a* modelling in the coastal sea of Zhejiang, China using GcTWR are presented in Sections 4 and 5. Furthermore, GcTWR is compared with global and other GWR-based models for performance examination. Finally, the study comes to an end with conclusions and summaries in Section 6.

2. Study area and data

2.1. Study area

The study area is situated in the Zhejiang coastal areas (ZCA) of the East China Sea (ECS), which is abundant in fishery resources and is a zone of frequent red tide events (Lou and Hu, 2014; Yang et al., 2013) (Fig. 1). It lies within a typical subtropical monsoon climate with four distinct seasons and is considerably affected by seasonal precipitation flows from the Yangtze River (Qiu et al., 2015), which results in strong seasonal variations in regional marine environmental processes. Every year, the Yangtze River transports about 240×10^6 t of sediment into the ECS, approximately 32% of which is stored in the ZCA and Fujian coastal region (Liu et al., 2006). In addition to the Yangtze River, several other rivers, including the Qiantang River, directly discharge

large quantities of freshwater with high nutrients and sediments into the ZCA (Cong et al., 2014; He et al., 2013).

Tidal action in the ZCA is powerful and causes significant resuspension of sediment, especially in the Hangzhou Bay, one of the strongest tidal bays in the world. As a result, the ZCA has optically complex water and significant seasonal variations, which makes the spatiotemporal heterogeneities of its marine processes quite complicated.

2.2. Dataset

In situ data used in this paper were collected by the Marine Monitoring and Forecasting Center of Zhejiang Province (Hangzhou, China) through survey cruises and dip samples. The study data covered time period from 2012 to 2016 and were collected four times each year in winter (March), spring (May), summer (July–August), and autumn (October) with exception in 2012 and 2013. The detailed information of the dataset is shown in Table 1.

The spatial distributions of monitoring stations were different every year and the number has increased from 214 in 2012 to 309 in 2016. The stations of 2016 were displayed in Fig. 1 and a total dataset of 4820 observations was available (Table 1). The dataset provided full water quality parameters, e.g., suspended matter (SM), potential of hydrogen (PH), salinity (SAL), chemical oxygen demand (COD), dissolved oxygen (DO), ammonia nitrogen (NH₃), nitrate nitrogen (NO₃), nitrite nitrogen (NO₂), silicate (SiO₄), phosphate (PO₄), total phosphorus (TP), total carbon (TC), total nitrogen (TN), Chl-*a*, etc. Moreover, it also contained geographic coordinates and monitoring date information to enable our spatiotemporal analysis.

In the analysis process, Chl-*a* concentrations were used as the dependent variable while the explanatory variables included a total of 25 variables. Through correctional and multicollinearity analysis using SPSS 22.0 (Table 2), we found that DO, COD, TN and PO₄ were the most strongly correlated parameters with Chl-*a*, and had the lowest value of variance inflation factor (VIF). In addition, DO and COD are known as important indicators of phytoplankton respiration strength, while TN and PO₄ are fundamental nutrient substances for phytoplankton growth (Cole and Harmon, 1981; Steingrund and Gaard, 2005). Therefore, DO, COD, TN and PO₄ were chosen as the independent variable in our experiment.

3. Geographically and cycle-temporally weighted regression modelling

3.1. GWR model

The basis for the GWR methodology is that parameters in each point are estimated locally ground on distance-weighted subsampling at neighbouring locations (Brunsdon et al., 1998; Fotheringham et al., 2002). GWR model that takes the version of the Ordinary Least Squares (OLS) model is presented as follows:

$$y_i = \beta_0(u_i, v_i) + \sum_k \beta_k(u_i, v_i)x_{ik} + \varepsilon_i \quad (1)$$

The index and coordinates of a spatial point are denoted as i and (u_i, v_i) in Eq. (1). Accordingly, y_i , x_{ik} and ε_i represent the dependent variable, the k th independent variable and the error term for the i th point, respectively. $\beta_0(u_i, v_i)$ is the intercept term, and $\beta_k(u_i, v_i)$ stands for the coefficient of k th independent variable at location i , which are permitted to vary across space to capture spatial nonstationarity. The estimator using matrix representation can be expressed as:

$$\hat{\beta}(u_i, v_i) = (X^T W(u_i, v_i) X)^{-1} X^T W(u_i, v_i) y \quad (2)$$

The $n \times n$ weights matrix associated with positions is represented by $W(u_i, v_i)$, with geographical weights in its leading diagonal and zeros in its off diagonal elements. A weighting function is established using the distance vector and a distance decay parameter such that neighbouring sample observations from the spatial data sample are allocated relatively more weight.

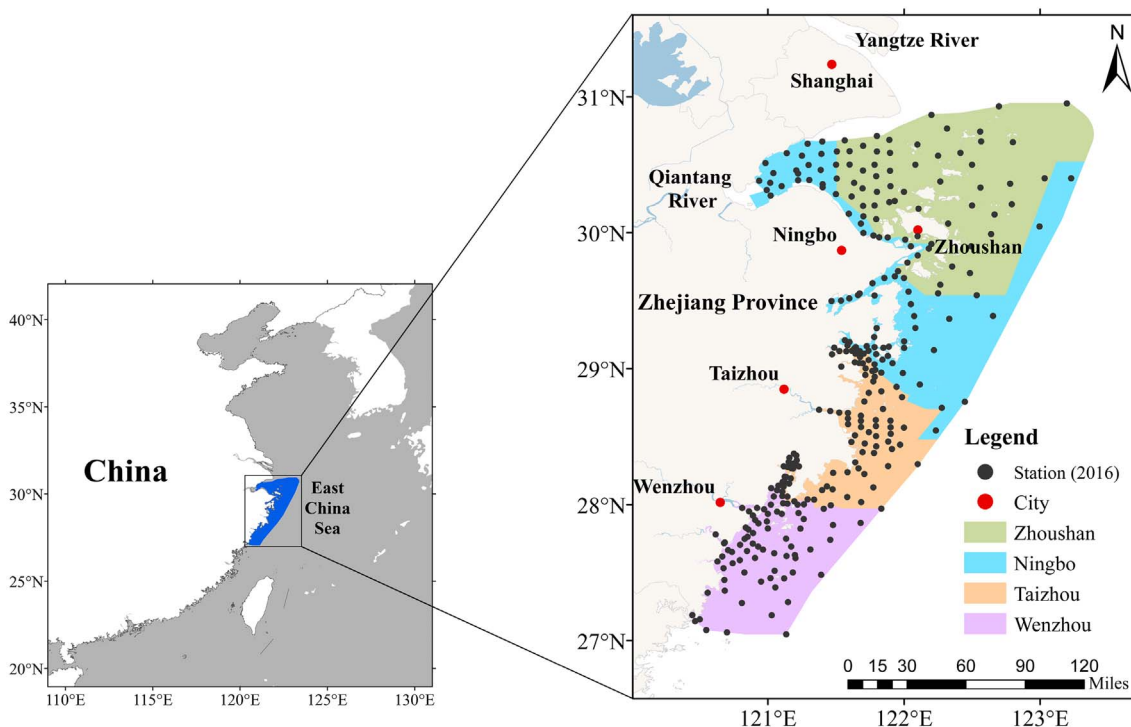


Fig. 1. Map of the study area in the Zhejiang coastal sea.

Table 1
Summary of the study dataset.

Year	Monitoring frequency	Stations	Observations
2012	2 (spring, summer)	214	428
2013	3 (spring, summer, autumn)	264	792
2014	4 (winter, spring, summer, autumn)	282	1128
2015	4 (winter, spring, summer, autumn)	309	1236
2016	4 (winter, spring, summer, autumn)	309	1236
Total	17	1378	4820

Table 2
Correctional and multicollinearity analysis of parameters.

	DO	COD	TN	PO ₄
R ² (Chl- <i>a</i>)	0.262 ^a	0.282 ^a	-0.178 ^a	-0.163 ^a
Sig.	0.000	0.000	0.000	0.000
VIF	1.085	1.062	1.005	1.119

^a Correlation is significant at the 0.01 level (2-tailed).

Gaussian-based, bi-square and tri-cube kernels are three most commonly used weighting functions, and each of them includes fixed and adaptive types. The distance in fixed kernel remains constant with varying quantity of nearest neighbours, while the quantity of neighbours in adaptive kernel is constant but the distance varies.

For example, the fixed Gaussian-based kernel function is form as follows:

$$W_{ij} = \exp(-d_{ij}^2/b^2) \tag{3}$$

where *b*, known as bandwidth, is a nonnegative decay parameter and generates an attenuation of impact related to the distance *d_{ij}*.

In practice, fixed kernel function is a proper selection for modelling when the samples are regularly spaced (Gollini et al., 2015). However, if the samples are dense or sparse, it is desirable to change the kernel size to fit the irregular patterns. Adaptive kernels with adaptive bandwidths are hence used to insure adequate local information for each local calibration (Fotheringham et al., 2002).

For instance, the adaptive bi-square weighting function can be expressed as:

$$W_{ij} = \begin{cases} [1 - (d_{ij}/b_i)^2]^2, & \text{if } d_{ij} < b_i \\ 0, & \text{otherwise} \end{cases} \tag{4}$$

where *b_i* represents the distance from position *i* to its *q*th nearest neighbour, i.e., the bandwidth of position *i*. Therefore, the calibration of adaptive kernel involves the estimation of *q* value (Fotheringham et al., 2002).

The bandwidth is calculated utilizing a cross-validation (CV) procedure:

$$CV(b) = \sum_i (y_i - \hat{y}_{\neq i}(b))^2 \tag{5}$$

In fact, by optimizing Eq. (5) according to the corrected Akaike Information Criterion (*AIC_C*), the parameter *b* or *q* is automatically fitted. *AIC_C* estimate takes the following form:

$$AIC_C = n \log_e(\hat{\sigma}^2) + n \log_e(2\pi) + n \left(\frac{n + tr(S)}{n - 2 - tr(S)} \right) \tag{6}$$

where *S* is the hat matrix. The fitted values \hat{y} are obtained by pre-multiplying the observed values *y* with matrix *S*:

$$\hat{y} = Sy \tag{7}$$

3.2. GcTWR model

3.2.1. GTWR model

GWR is essentially an approach of “borrowing” data from ambient positions for modelling spatial nonstationarity alone. Due to the fact that time is as well a fundamental attribute belonging to geographic processes, Huang et al. (2010) produced a GTWR model by constructing a spatiotemporal weight matrix to account for spatiotemporal nonstationarity. The GTWR model is presented as:

$$y_i = \beta_0(u_i, v_i, t_i) + \sum_k \beta_k(u_i, v_i, t_i)X_{ik} + \varepsilon_i \tag{8}$$

The estimates of $\beta_k(u_i, v_i, t_i)$ similarly takes the following form:

$$\hat{\beta}(u_i, v_i, t_i) = (X^T W(u_i, v_i, t_i) X)^{-1} X^T W(u_i, v_i, t_i) y \tag{9}$$

The spatiotemporal weight matrix is denoted as $W(u_i, v_i, t_i)$, based on the definition of the spatiotemporal distance and its decay functions.

Considering that location and time usually have different scaling effects, Huang et al. (2010) combined the spatial distance d^S and the temporal distance d^T to form a spatiotemporal distance $d^{ST} = d^S \otimes d^T$, with symbol \otimes standing for different operators. If operator ‘+’ is accepted, the spatiotemporal distance d^{ST} is a linear combination of d^S and d^T as follows:

$$d^{ST} = \lambda d^S + \mu d^T \tag{10}$$

where λ and μ are scale parameters to counterbalance the dissimilar influences between d^S and d^T .

3.2.2. Extending GTWR with cycle-temporal variations

Despite the fact that space and time are two fundamental dimensions pertaining to marine environmental processes, seasonal periodicity is also a significant attribute in marine environmental processes. The variations of Chl-a in several typical monitoring stations were depicted from 2012 to 2016 (Fig. 2). According to the time-series curves, Chl-a demonstrated both seasonal and interannual characteristics, but the former was strong and the latter was not significant.

Considering that Chl-a variations are composed of interannual and seasonal portions, the time variable T is divided into seasonal periodic and interannual aperiodic parts:

$$T = T_c + T_{nonc} \tag{11}$$

where T_c is the seasonal periodic part, i.e., the period within the year of the monitoring date; T_{nonc} is the interannual aperiodic part, i.e., the year part of the monitoring date.

For example, we have two stations named A and B, and the monitoring date of A is ‘2015/05/15’ while that of B is ‘2016/09/18’. According to the definition, the T_c of A and B are ‘05/15’ and ‘09/18’, and the T_{nonc} of them are ‘2015’ and ‘2016’. Therefore, the temporal distance d_{AB}^T , the cyclical temporal distance $d_{AB}^{T_c}$, and the noncyclic temporal distance $d_{AB}^{T_{nonc}}$ from A to B can be calculated as follows:

$$d_{AB}^{T_c} = T_c(B) - T_c(A) = |09/18 - 05/15| = 126 \text{ days}$$

$$d_{AB}^{T_{nonc}} = T_{nonc}(B) - T_{nonc}(A) = |2016 - 2015| = 1 \text{ year} = 365 \text{ days}$$

$$d_{AB}^T = d_{AB}^{T_c} + d_{AB}^{T_{nonc}} = 491 \text{ days}$$

where $| |$ represents the absolute value. Given that T_c and T_{nonc} may have different scaling and intensity effects, a symbol \oplus is introduced to structure the temporal distance d^T as below:

$$d^T = d^{T_c} \oplus d^{T_{nonc}} \tag{12}$$

where different operators can be adopted to replace the symbol \oplus . Therefore, the total spatiotemporal distance d^{ST} of GcTWR is expressed as:

$$d^{ST} = d^S \otimes d^T = d^S \otimes (d^{T_c} \oplus d^{T_{nonc}}) \tag{13}$$

If both the spatiotemporal distance d^{ST} and temporal distance d^T are measured by the ‘+’ operator, the Eq. (13) is expressed as follows:

$$d^{ST} = \lambda d^S + \mu(\varphi d^{T_c} + \delta d^{T_{nonc}}) \tag{14}$$

where λ , μ , φ , and δ are scale parameters to balance the influences between space and time.

According to Eq. (14), if the Euclidean distance is adopted, the spatiotemporal distance d_{ij}^{ST} between point i and point j is calculated as below:

$$d_{ij}^{ST} = \lambda[\sqrt{(u_i - u_j)^2 + (v_i - v_j)^2}] + \mu(\varphi |t_{ci} - t_{cj}| + \delta |t_{nonci} - t_{noncj}|) \tag{15}$$

where t_{ci} and t_{nonci} are the periodic and aperiodic temporal components at position i while t_{cj} and t_{noncj} are the same components at position j .

If the Gaussian decline-based function is adopted, a space-time weight can be structured as follows:

$$\begin{aligned} w_{ij}^{ST} &= \exp\left\{-\left(\frac{\lambda[(u_i - u_j)^2 + (v_i - v_j)^2] + \mu\varphi(t_{ci} - t_{cj})^2 + \mu\delta(t_{nonci} - t_{noncj})^2}{h_{ST}^2}\right)\right\} \\ &= \exp\left\{-\left(\frac{(u_i - u_j)^2}{h_S^2} + \frac{(v_i - v_j)^2}{h_T^2} + \frac{(t_{ci} - t_{cj})^2}{h_{T_c}^2} + \frac{(t_{nonci} - t_{noncj})^2}{h_{T_{nonc}}^2}\right)\right\} \\ &= \exp\left\{-\left(\frac{(d_{ij}^S)^2}{h_S^2} + \frac{(d_{ij}^{T_c})^2}{h_{T_c}^2} + \frac{(d_{ij}^{T_{nonc}})^2}{h_{T_{nonc}}^2}\right)\right\} \\ &= \exp\left\{-\frac{(d_{ij}^S)^2}{h_S^2}\right\} \times \exp\left\{-\frac{(d_{ij}^{T_c})^2}{h_{T_c}^2}\right\} \times \exp\left\{-\frac{(d_{ij}^{T_{nonc}})^2}{h_{T_{nonc}}^2}\right\} \\ &= w_{ij}^S \times w_{ij}^{T_c} \times w_{ij}^{T_{nonc}} \end{aligned} \tag{16}$$

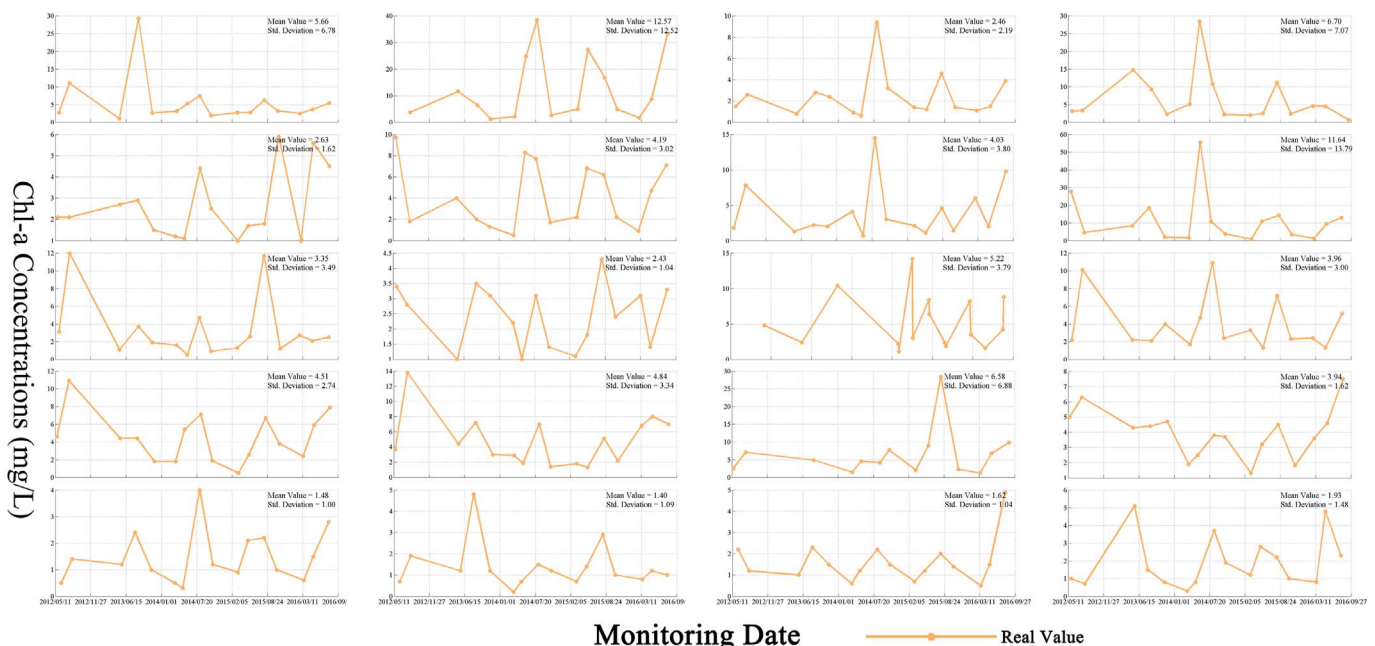


Fig. 2. Chl-a trends at selected monitoring stations from 2012 to 2016.

Table 3
ANOVA comparison between GWR-based and global regression models.

Models	RSS	MS	F	p-Value	R ²	Adjusted R ²	AIC	Bandwidth or q value	μ/λ	φ/δ
OLS	215,830.00	43,166.00	/	/	0.2942	0.2910	26,580.20	/		
GWR ¹	127,484.20	35.48	9.02	0.00	0.5241	0.5218	25,267.38	146		
GWR ²	109,523.49	32.87	6.02	0.00	0.5911	0.5892	24,874.97	12,801.29		
cTWR	94,682.11	27.32	10.98	0.00	0.6465	0.6449	24,168.15	8342.18		23.611
GTWR	31,569.85	13.89	8.31	0.00	0.8721	0.8715	22,792.04	23,838.19	4.333	
GcTWR	22,151.93	10.84	9.79	0.00	0.9274	0.9270	22,592.21	26,583.87	3.286	24.286

GWR¹: GWR model with adaptive kernel; GWR²: GWR model with fixed kernel; RSS: residual sum of squares; MS: mean square.

Afterwards, the weight matrix $W(u_i, v_i, t_i)$ of GcTWR containing the spatial-temporal weights in its leading diagonal and zeros in its off-diagonal elements is calculated as follows:

$$W(u_i, v_i, t_i) = \begin{bmatrix} w_{j_0}^S \times w_{j_0}^{T_c} & 0 & 0 & 0 \\ \times w_{j_0}^{T_{nonc}} & & & \\ 0 & w_{j_1}^S \times w_{j_1}^{T_c} & 0 & 0 \\ & \times w_{j_1}^{T_{nonc}} & & \\ 0 & 0 & \dots & 0 \\ 0 & 0 & 0 & w_{in}^S \times w_{in}^{T_c} \times w_{in}^{T_{nonc}} \end{bmatrix} \quad (17)$$

Following Eq. (15), if temporal nonstationarity is out of consideration in the study area, the parameter μ is set as 0, which is equal to the conventional GWR distance. In contrast, if parameter λ is set as 0, temporal nonstationarity, including periodic and aperiodic parts, are taken into consideration. This leads to a cycle-temporally weighted regression model (cTWR). If both μ and δ are set as 1, a GTWR model similar to the model proposed by Huang et al. (2010) is achieved.

In practice, however, none of the parameters ($\lambda, \mu, \phi, \delta$) equals to zero in most real situations. In this research, λ and δ are set to 1 to simplify parameter estimations without losing generalization, so only μ and ϕ need to be calibrated and optimised through the CV procedures according to the AIC_C.

3.3. Implementation of the proposed method

Monitoring data from 2012 to 2016 in the Zhejiang coastal sea of China was used in this paper. The original data were transformed from geographic coordinate system to projected coordinate system of ‘Xian_1980_3_Degree_GK_CM_120E’, and their monitoring dates were converted to Julian day count. Therefore, the space and time units adopted in our experiments were meter and day. Considering the numerical ranges of space, cyclic-time, and noncyclic-time distances were quite difference, we regularized and converted the time distances to the extent of space distances as follows:

$$d_{convert}^T = (d_{origin}^T - d_{min}^T) \times (d_{max}^S - d_{min}^S) + d_{min}^S \quad (18)$$

where d_{min}^S and d_{max}^S are the minimum and maximum values of space distance. d_{min}^T , d_{origin}^T , and $d_{convert}^T$ are the minimum, original, and converted time distances. The d_{origin}^T can be denoted by cyclic-time, noncyclic-time and total-time distances.

Six different regression models, namely, the global OLS, two conventional GWR models of adaptive and fixed Gaussian-based kernels (GWR¹ and GWR²), the proposed cTWR, GTWR and GcTWR, were performed on the dataset for Chl-*a* prediction. The analysis of variance (ANOVA) tests suggested by Brunson et al. (1999) were adopted here to compare their estimation results in Table 3.

In the ANOVA table, the residual sums of squares (RSS) of various models are displayed in the first column and the second column presents the mean square (MS). The p-values and the pseudo-F estimates are shown in the third and fourth columns, along with R² and adjusted R² in the fifth and sixth columns. In addition, the AIC and bandwidth (fixed kernel) or q (adaptive kernel) values are presented in the next

two columns. The last two columns are the ratios of space-time (μ/λ) and cyclic-noncyclic temporal (ϕ/δ) scale parameters, respectively.

3.4. Parameter selection

Considering that location and time usually have different scaling effects, similar to T_c and T_{nonc} , we introduced parameters λ, μ, ϕ , and δ to balance the differences between spatial and temporal units. Then, we reduced the count of parameters in practice by setting $\lambda = \delta = 1$ such that just μ and ϕ have to be estimated.

In our study, a validation procedure is used to optimize the μ and ϕ values according to R² and AIC. The optimization of validation procedure includes three steps:

- (1) Firstly, minimize the AIC value to achieve the optimal bandwidth b and return R_b^2 for all fixed μ and ϕ values;
- (2) Then, vary the ϕ value and repeat step (1) to maximize the R_ϕ^2 for all fixed μ value;
- (3) At last, vary the μ value and repeat step (2) to maximize the R_μ^2 .

The optimization process can also be displayed as follows:

$$F(\mu, \phi, b) = \max R_\mu^2 (\max R_\phi^2 (\min AIC_b)) \quad (19)$$

where $\max X_\alpha$ and $\min X_\alpha$ means maximizing or minimizing the X value by optimizing the value of α .

The validation procedure is implemented in Matlab 2013a and a one-dimensional minimizer function $fminbnd$ that finds the minimum is used to solve the scalar problem and conduct the optimization. Considering that $\max R^2 \equiv \min (1 - R^2)$, Eq. (19) is realized in Matlab as below:

$$F(\mu, \phi, b) = fminbnd(1 - R_\mu^2)(fminbnd(1 - R_\phi^2)(fminbnd(AIC_b))) \quad (20)$$

The results of parameters μ and ϕ against R² acquired by validation procedures are represented by Fig. 3. We notice that the maximal R² = 0.9274 is attained when $\mu = 3.286$ and $\phi = 24.286$.

To compare the periodic and aperiodic time effects more intuitively, we set $\mu = 3.286$ and vary the value of ϕ to observe the change of R² using CV procedures. Selection details of parameter ϕ are presented in Fig. 4. When ϕ is smaller than the optimal value (24.286), R² increases with the growth of ϕ ; after the optimal value, it decreases smoothly. In addition, the result also shows that when choosing an ineffective ϕ parameter, the explanatory power of the GcTWR model could be poorer than GTWR. For example, when $\mu = 3.286$, if $\phi > 45$, the R² of GcTWR is less than that of optimal GTWR, where R² = 0.8721.

4. Results

4.1. Global OLS model

We implemented the global OLS model on the collected dataset to investigate the average relationships between Chl-*a* concentrations and the selected factors (Table 4). The results show that only 29.42% of the

Fig. 3. The parameters μ and φ against R^2 statistics.

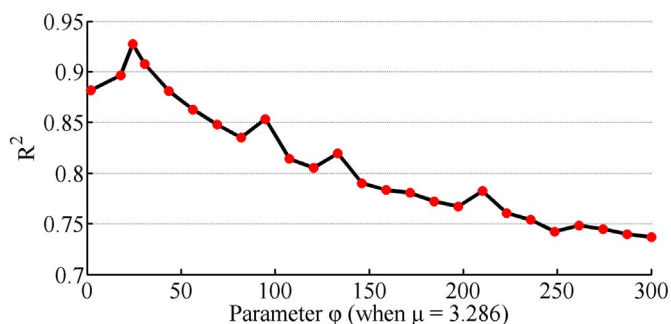
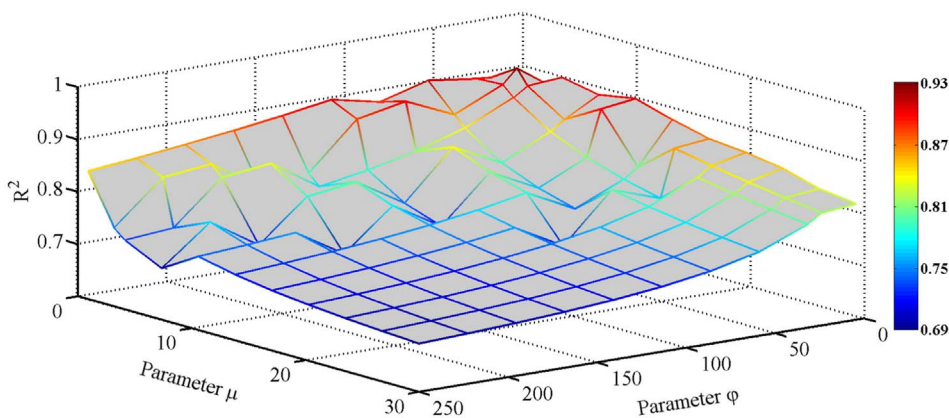


Fig. 4. R^2 values plotted against parameter φ when $\mu = 3.286$.

Table 4
OLS model parameter estimate summaries.

Variable	Coefficient	Std. deviation	t-Statistic	Sig.
Constant ^a	-1.657	0.544	-3.045	0.002
DO ^a	1.886	1.321	14.279	0.000
COD ^a	2.298	1.194	19.246	0.000
TN ^a	-9.713	0.763	-12.730	0.000
PO ₄ ^a	-4.558	3.655	-12.470	0.000
Diagnostic information				
R^2	0.2942			
Residual standard error (RSE)	7.4650			
Residual sum of squares (RSS)	215,830.00			
AIC	26,580.20			

^a Indicates 1% statistical significance.

Chl-*a* concentration variance is explained by the global model in term of R^2 . Nonetheless, according to the t-probabilities, all independent variables, including DO, COD, TN, and PO₄, are statistically significant

Table 5
GWR and cTWR parameter estimate summaries.

Parameter	GWR (bandwidth = 12,801.29)			cTWR (bandwidth = 8342.18)		
	Min	Med	Max	Min	Med	Max
Constant	-4.852	0.402	4.220	-5.364	4.048	11.707
DO	-3.645	3.403	10.441	-19.495	1.192	16.487
COD	-1.941	4.614	11.294	-10.454	0.203	10.725
TN	-1.151	2.005	4.462	-6.862	-1.030	4.724
PO ₄	-11.219	-6.807	1.340	-10.593	-1.253	11.866
Diagnostic information						
R^2		0.5911			0.6465	
RSE		5.3178			4.9442	
RSS		109,523.49			94,682.11	
AIC		24,874.97			24,168.15	

at 99.5% confidence level. In addition, DO and COD are positively associated with Chl-*a*, while TN and PO₄ are negatively correlated with Chl-*a*.

4.2. GWR-based models

GWR, cTWR, GTWR, and GcTWR models were performed on the same dataset. The estimations are presented in Tables 5 and 6. Considering the results of local parameter estimates are massive, the distributions of parameters are simply shown by a three-column outline to imply their variability.

The proportion of variance interpretation has risen from 29.42% in OLS to 59.11% in GWR, 64.65% in cTWR, 87.21% in GTWR, and 92.74% in GcTWR. The significantly reduced RSS and residual standard error (RSE) values in cTWR and GWR over OLS respectively indicate the strong spatial heterogeneity and temporal heterogeneity in our dataset. GTWR, on the other hand, obtains better result than GWR and cTWR due to the fact that it manages both spatial and temporal non-stationarities. Furthermore, after considering the cycle-temporal variations on the basis of GTWR, GcTWR acquires the most superior performance according to AIC and R^2 .

4.3. Results of spatiotemporally heterogeneous chlorophyll-*a*

4.3.1. Spatiotemporal heterogeneity of Chl-*a*

One significant advantage of the GWR-based methods is that the local estimated results of parameters are mappable and viewable by different colours and symbol sizes proportional to their absolute values. For example, the spatial distributions of DO estimations in the spring of 2015 using the GWR, GTWR, and GcTWR models are shown in Fig. 5. We can see significant spatial variations over the study area in all models, and the distribution patterns of GTWR-based (GTWR and GcTWR) models present more aggregation phenomena than GWR model.

Table 6
GcTWR and GTWR parameter estimate summaries.

Parameter	GcTWR (bandwidth = 26,583.87)			GTWR (bandwidth = 23,838.19)		
	Min	Med	Max	Min	Med	Max
Constant	-8.108	-3.001	2.577	-1.503	0.013	1.780
DO	-2.204	1.077	4.128	-5.278	1.043	3.348
COD	-2.389	8.015	15.173	-3.342	0.067	3.748
TN	-10.740	-3.000	2.170	-9.294	3.012	14.256
PO ₄	-2.694	4.005	12.904	-14.754	-2.119	6.801
Diagnostic information						
R ²		0.9274			0.8721	
RSE		2.3915			2.8550	
RSS		22,151.93			31,569.85	
AIC		22,592.21			22,792.04	

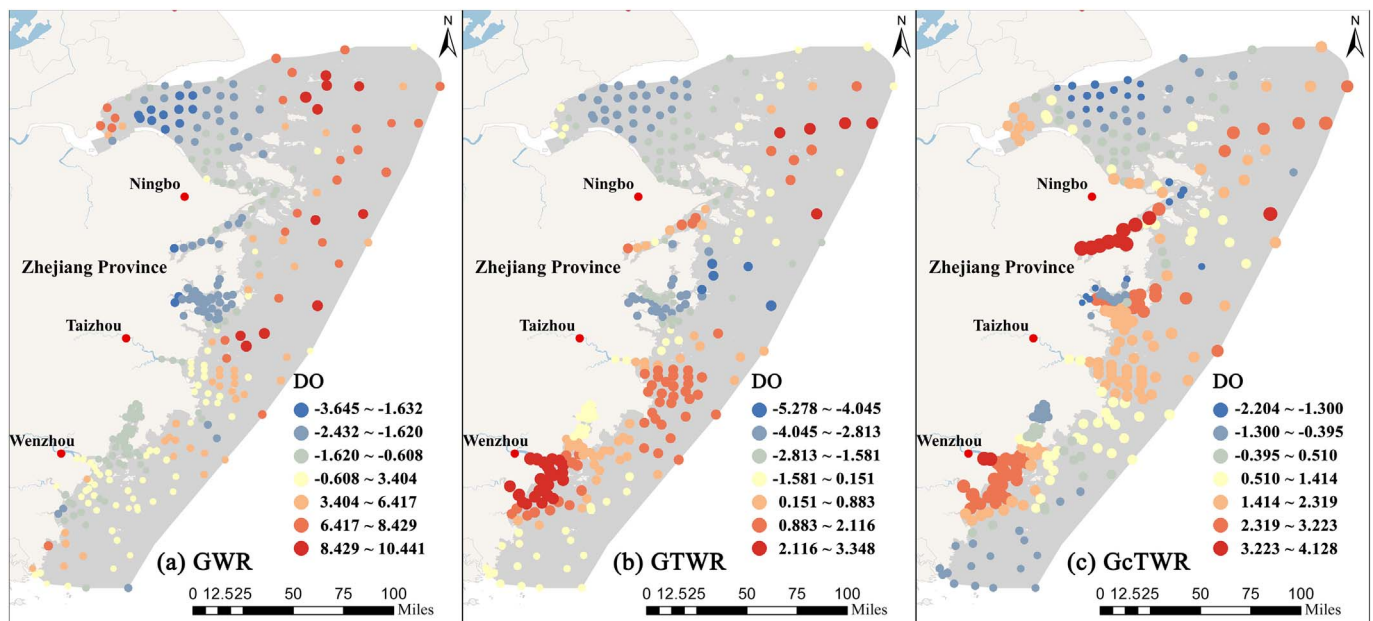


Fig. 5. Parameter estimates of DO in spring of 2015 using GWR, GTWR, and GcTWR. (For interpretation of the references to colour in this figure legend, the reader is referred to the web version of this article.)

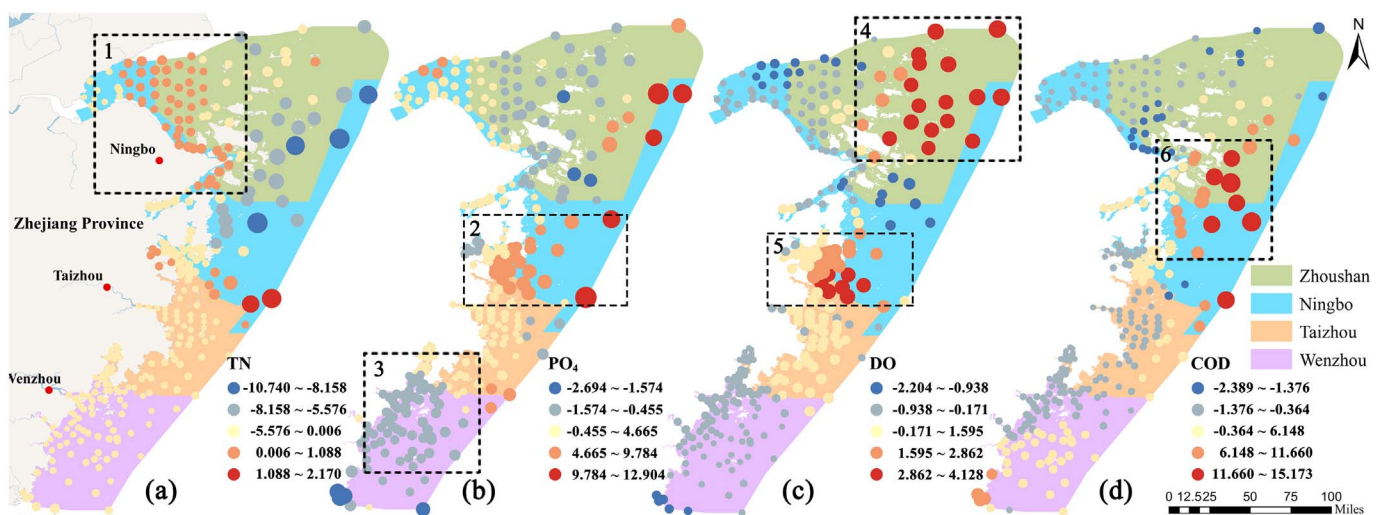


Fig. 6. Spatial variation of TN, PO₄, DO and COD coefficients.

Diverse distributions of parameters indicate that the spatial effects vary across space. For instance, the spatial variation of TN, PO₄, DO, and COD in the spring of 2016 obtained by GcTWR are shown in Fig. 6. TN shows significant positive influence on Chl-*a* in the Hangzhou Bay area (Fig. 6a, Region

1). PO₄, however, shows strong positive influences on Chl-*a* in the Ningbo sea areas (Fig. 6b, Region 2) but negative effects in the Wenzhou sea areas (Fig. 6b, Region 3). In addition, we can see that DO has the most significant effects in the Zhoushan (Fig. 6c, Region 4) and Ningbo (Fig. 6c, Region 5) sea

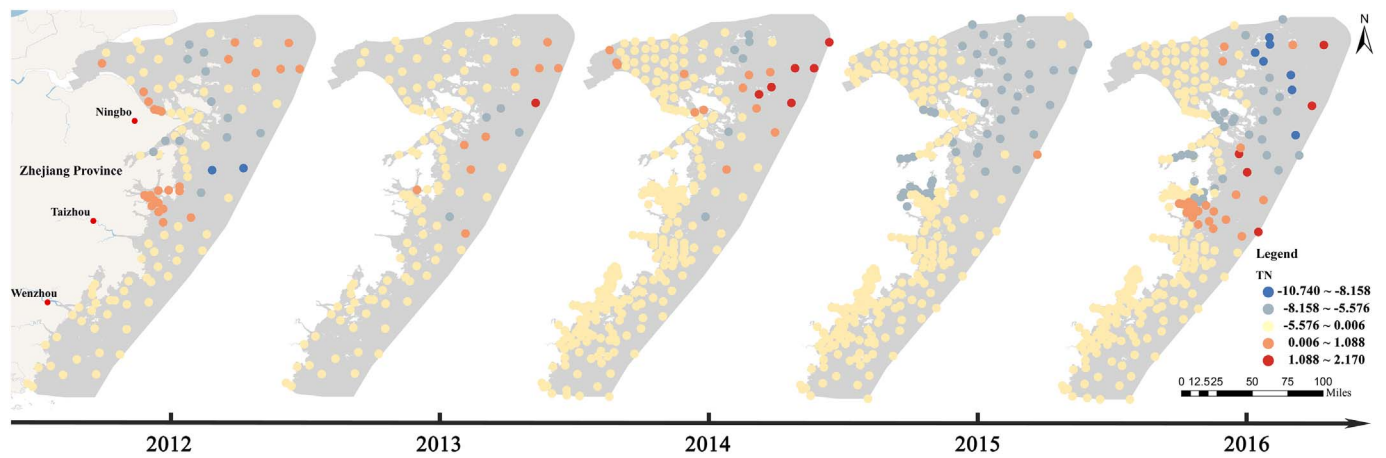


Fig. 7. Spatiotemporal distributions of TN in summer from 2012 to 2016.

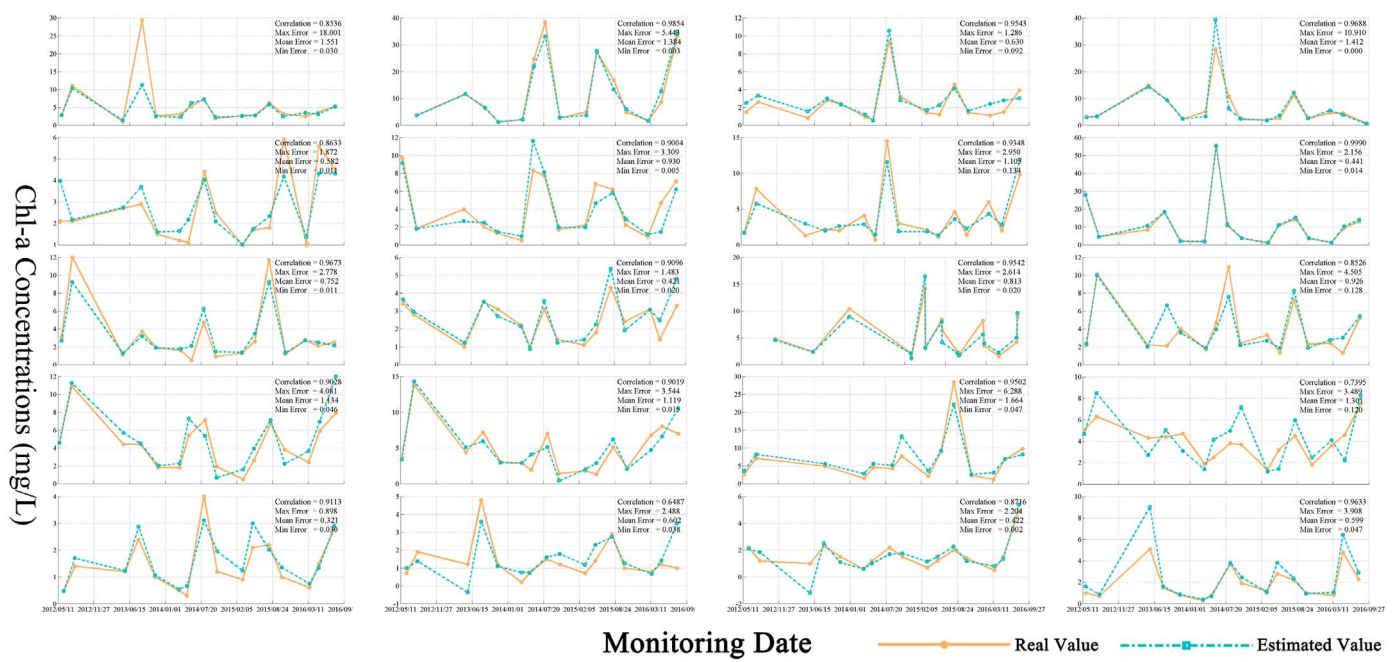


Fig. 8. Comparison between real values and estimated values at selected monitoring stations from 2012 to 2016.

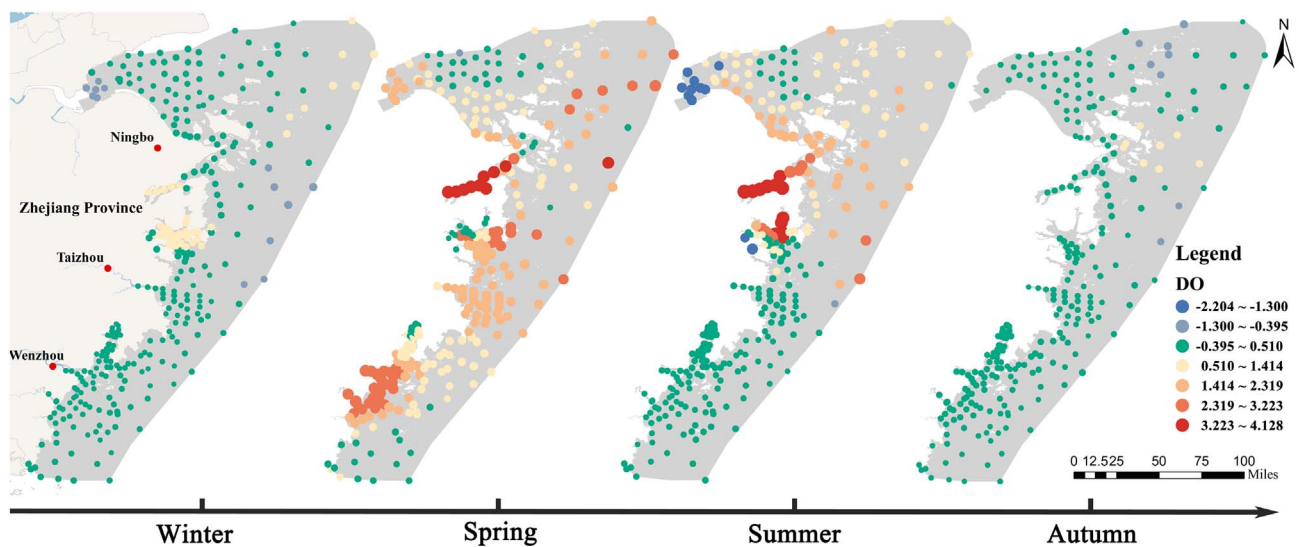


Fig. 9. Spatiotemporal seasonal variations of parameter DO.

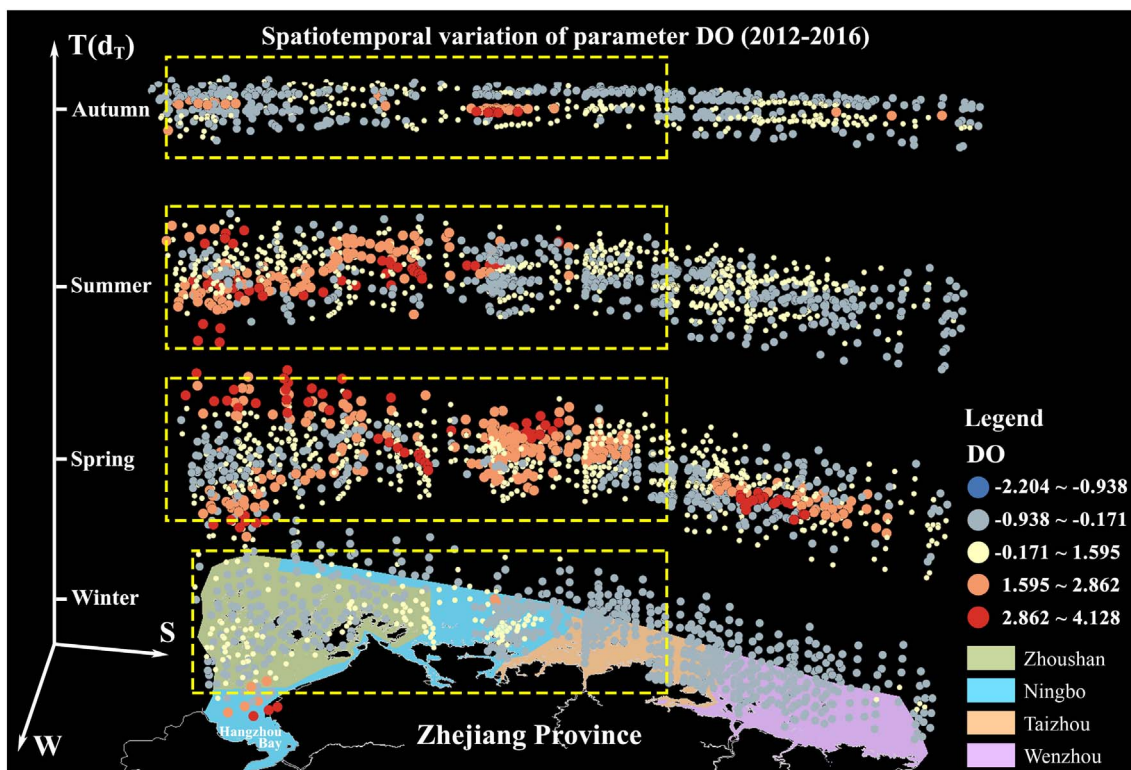


Fig. 10. Spatiotemporal variation of parameter DO with 3D representation.

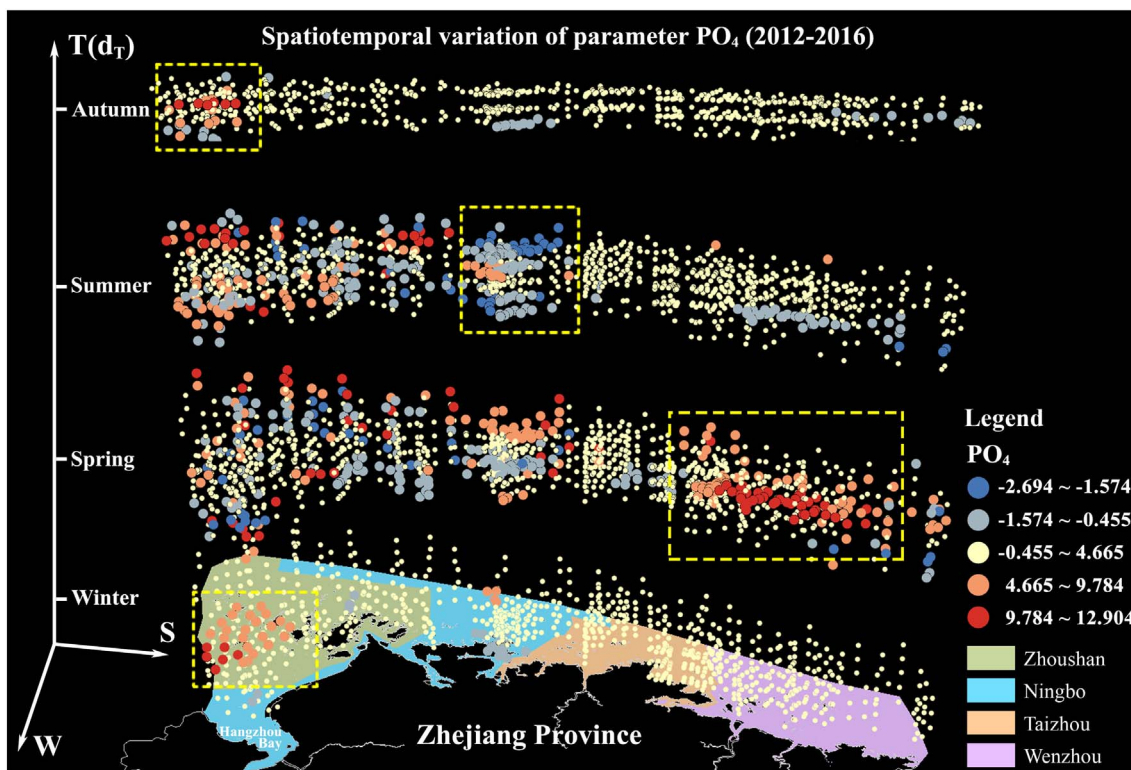


Fig. 11. Spatiotemporal variation of parameter PO₄ with 3D representation.

areas, and COD has the most powerful influences in the Ningbo sea areas (Fig. 6d, Region 6). Given that spring is the season of high red tide incidences in the ZCA, these results suggest that by controlling specific parameters in different sea areas, the variations of Chl-a can be changed and the red tides might be mitigated.

By comparing the spatial distributions of parameter TN in summer

from 2012 to 2016 using GcTWR (Fig. 7), we note that the five years' results are almost identical except for some minor differences which may be caused by the year-to-year modifications in monitoring stations and monitoring time. It further demonstrates that the interannual effects of parameter TN on Chl-a are non-significant.

In addition, the spatial distributions of all parameters (TN, DO, COD and

PO₄) in all 17 seasons from 2012 to 2016 are displayed in Appendix A. In the results, the spatial distributions of parameter TN in other seasons or the spatial variations of other parameters in a specific season show similar spatial patterns. Besides, the estimations present similar distributions in 2014, 2015 and 2016, while in 2012 and 2013, the distribution patterns are slightly different. The difference of the distributions and quantities of monitoring stations between 2014–2016 and 2012–2013 are very likely to be the reason behind the phenomenon.

4.3.2. Cycle-temporal nonstationarity over seasons

Strong seasonal characteristics are discovered after analysing Chl-*a* variations of several typical monitoring stations in Fig. 2. To evaluate the capacity of GcTWR for modelling the seasonal variations, the estimated Chl-*a* values of GcTWR are compared with the real values in Fig. 8. The almost identical temporal trends of both values in all stations indicated that the seasonal nonstationarity are fully captured by the GcTWR model.

Significant cycle-temporal variability of Chl-*a* is also verified by the variations of parameter DO over seasons in 2015 (Fig. 9). Parameter DO demonstrates relatively analogous spatial distribution in spring and summer; while in autumn and winter, the distribution patterns are remarkably different. Particularly, due to the more suitable weather conditions for phytoplankton growth in spring and summer in the ZCA, the influences of DO on Chl-*a* in these two seasons are more active than that in autumn and winter. It accordingly explains the reason why spring and summer are the frequent occurrence periods of red tide. For other parameters, the spatial distributions over seasons are observable from Figs. 12 to 15 in Appendix A, which as well demonstrate significant variability over seasons.

5. Discussion

5.1. Applicability of the GcTWR model

Geographic and environmental processes often present nonstationarity among both time and space. This phenomenon is especially complicated in marine environmental process with significant seasonal variations (Wang et al., 2015). In this paper, we put forward an innovative model called GcTWR on the basis of the GTWR model of Huang et al. (2010). It divides temporal distance into seasonal periodic and interannual aperiodic parts to deal with the spatiotemporal nonstationarity and seasonal variations simultaneously. The application of GcTWR in Chl-*a* modelling using a 2012–2016 dataset in Zhejiang coastal areas, along with the comparison with the traditional OLS and GWR-based approaches, demonstrates the effectiveness and efficiency of the proposed model (Table 3).

Compared with the widely used global regression model (OLS), both local spatial (GWR) and temporal model (cTWR) present considerable improvement in performance according to the reductions in RSS and increase in R², which confirms that the relationships between Chl-*a* concentrations and four explanatory variables (DO, COD, TN, and PO₄) are characterized by significant spatial and temporal nonstationarity. Also, we note that the performance of GWR² is much better than GWR¹ in term of RSS and R², which indicates that the fixed kernel is superior to the adaptive kernel for our dataset. Therefore, the fixed kernels are adopted in the cTWR, GTWR and GcTWR models. Compared with traditional global and local (spatial or temporal) models, the GTWR and our proposed GcTWR models perform much better in term of all statistical indicators (Table 3), probably due to their capability to account for the nonstationarity in both space and time. Studies have shown that seasonal variations in marine environment are quite significant (Chen and Liu, 2015; Khodse et al., 2007). Consequently, after considering the cycle-temporal variations on the basis of GTWR, GcTWR acquires the most superior performance, which further testifies the applicability and efficiency of GcTWR model.

Small bandwidths usually indicate more rapid variations among time or space while large bandwidths are more similar to the universal model (Gollini et al., 2015). Given that the temporal distances have converted to the same range of spatial distances in the modelling, the bigger bandwidth of GWR² over cTWR model indicates that the temporal variation in our dataset is more

obvious than the spatial variation. When comparing the bandwidths of GTWR-based models which address both spatial and temporal heterogeneities, GTWR model shows more rapid variation than GcTWR model.

In the meantime, we find that the cyclic-noncyclic ratios (φ/δ) in cTWR and GcTWR models are far > 1, reaching up to 23.611 and 24.286. Considering that d_c^T and d_{nonc}^T are under the same metric system, it further demonstrates that the seasonal influences of Chl-*a* are much more significant than the interannual effects. This conclusion is also verified by the significant cycle-temporal variability observed from the spatiotemporal distribution of estimations in Fig. 9 and Appendix A.

In addition, Chl-*a* is the biological indicator of coastal environments. The information of spatial distribution provided by the GcTWR model is useful for developing more effective plans and policies for environmental protection and pollution, such as mitigate the negative effects of red tides according to the results of Fig. 6.

5.2. Analysis of spatiotemporal nonstationarity using 3D visualization

To present the spatial distribution and temporal variation concurrently are quite important for the analysis of space-time models (Kraak and Koussoulakou, 2005). Therefore, a novel 3D visualization method is proposed in this paper to show the spatiotemporal heterogeneity and seasonal variations more directly and intuitive for GcTWR model.

We use longitude as the X-axis towards the south and latitude as the Y-axis towards the west. d^T ($d^T = \varphi d^{Tc} + \delta d^{Tnonc}$) is used as the Z-axis, and φ and δ are the optimal parameters of GcTWR, i.e., $\varphi = 24.286$ and $\delta = 1$. The 3D representation of parameters DO and PO₄ are shown in Figs. 10 and 11.

Since φ is considerably larger than δ , d^T is primarily controlled by d^{Tc} and reveals seasonal clustering on the Z-axis. Moreover, the slight difference of monitoring times in each season during the five years leads to unobvious stratifications among the same seasons. Compared to Fig. 9, Fig. 10 portrays the spatiotemporal variations of parameter DO in more details over time. From the perspective of 3D visualization, it represents the spatiotemporal nonstationarity and aggregation more intuitively. We notice Fig. 10 that the influences of DO on Chl-*a* have significant spatiotemporal characteristics in the Zhoushan, Ningbo and Taizhou sea areas (ZNTSA, selected by the yellow frames). In winter, DO shows a smoothly negative influence in the ZNTSA; however, the influence suddenly turns strongly positive in spring. In summer, there are both positive and negative influences, and the positive forces are dominant. In autumn, however, the impact is mainly controlled by the negative forces, and the positive effects decrease rapidly.

In addition, some obvious spatiotemporal aggregation phenomena are noted in Fig. 11. For example, there are positive clusters in the Wenzhou sea areas in spring; and strong negative aggregations appear in the Ningbo sea areas in summer (selected by the yellow frames).

6. Conclusions

In this study, a GcTWR model extending GTWR with cycle-temporal variations was put forward to incorporate seasonal variations into spatiotemporal heterogeneity in the marine environmental processes in coastal areas. The proposed model could be applied to manage both spatial and cycle-temporal nonstationarity for similar phenomena with periodicity characteristics, such as human activities, social events, and environmental processes.

The experimental results of Chl-*a* in the Zhejiang coastal areas demonstrate that GcTWR obtains an excellent goodness of fit and adequate spatiotemporal explanatory capability compared to the GWR, cTWR, and GTWR models. In the comparisons among the GWR-based and global models, the R² of OLS, GWR, cGWR and GTWR are improved from 0.2942, 0.5911, 0.6465 and 0.8721, respectively, to 0.9274 by GcTWR. Absolute errors are reduced in OLS, cTWR, GWR and GTWR by 89.74%, 79.77%, 76.60% and 29.83% relative to the GcTWR model. The results of ANOVA tests and AIC statistics illustrate the same substantial improvements. Consequently, we come to the conclusion that it is significant to extend GTWR with cycle-temporal variations.

Limitations, however, still remain in our research. For instance, a simple linear combination is adopted to construct both temporal distance and total spatiotemporal distance in our method while more effective combination schemes should be explored in the future. Additionally, marine environmental processes are complex and affected by ocean dynamics and physical oceanography. Therefore, we will attempt to combine GcTWR model with ocean dynamics models to improve the performance.

Appendix A

Funding

Public Science and Technology Research Projects (201305012, 201505003); Special Program for National Basic Research (2012FY112300).

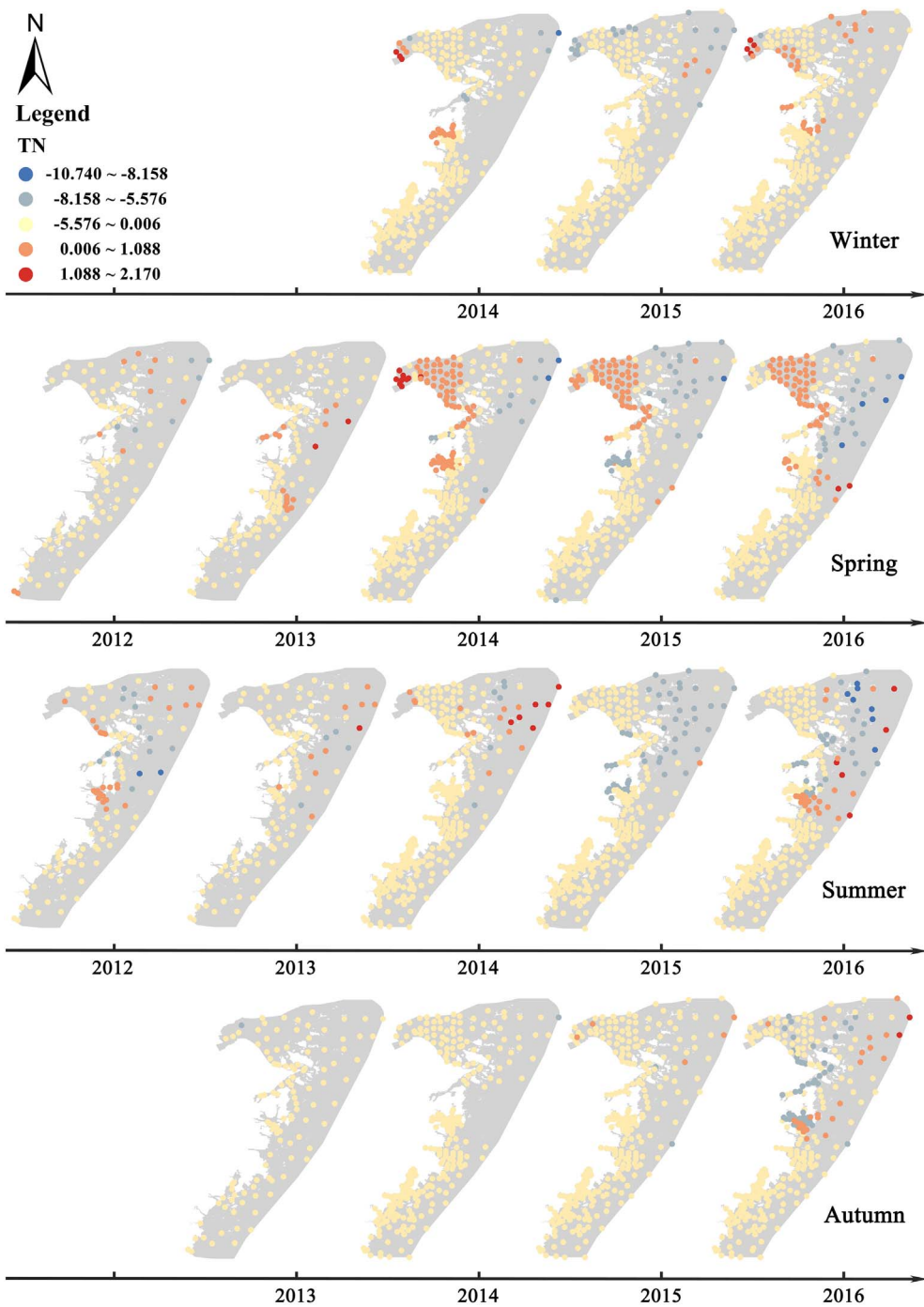


Fig. 12. Spatiotemporal distributions of parameter TN in all (totally 17) seasons from 2012 to 2016.

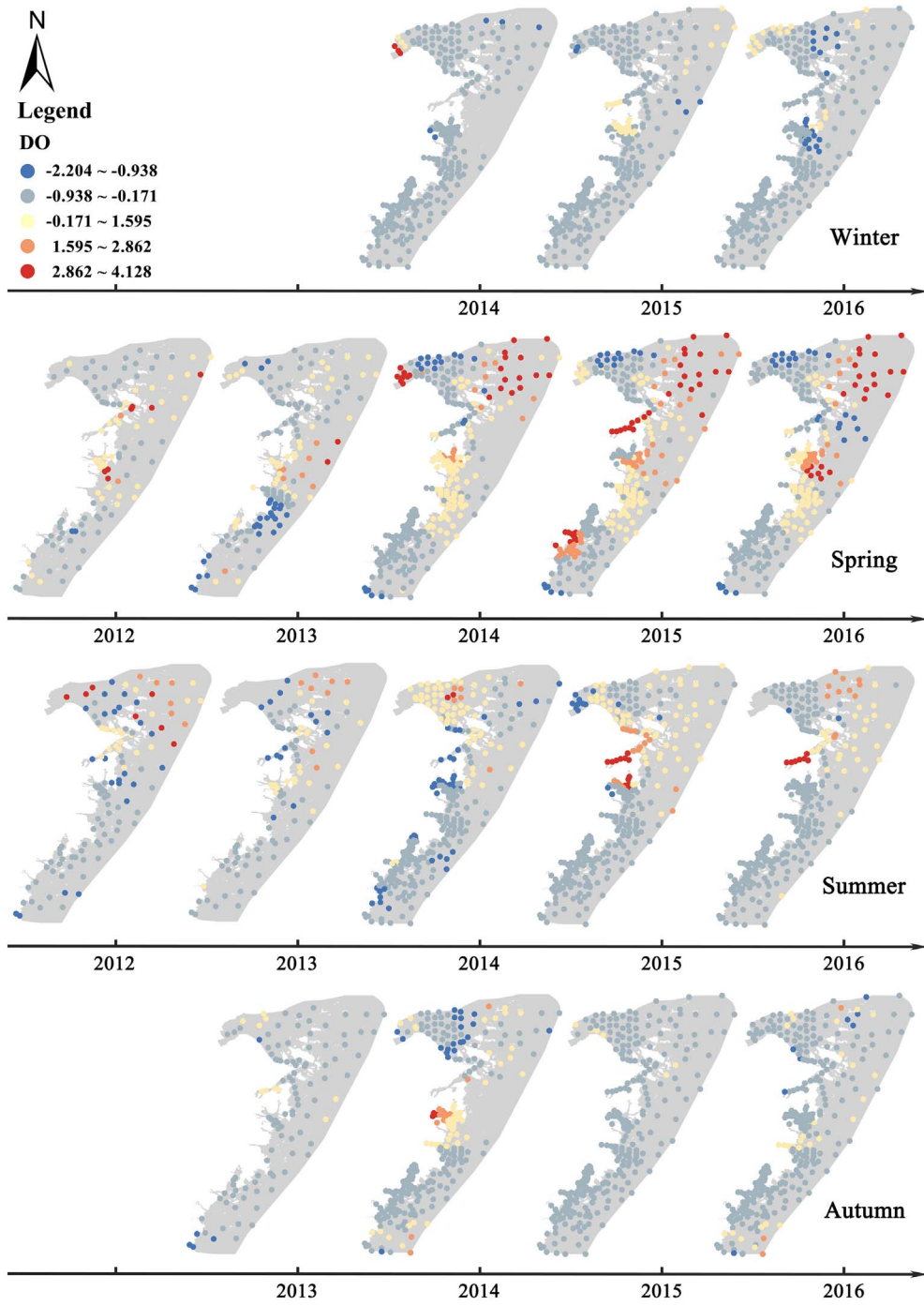


Fig. 13. Spatiotemporal distributions of parameter DO in all (totally 17) seasons from 2012 to 2016.

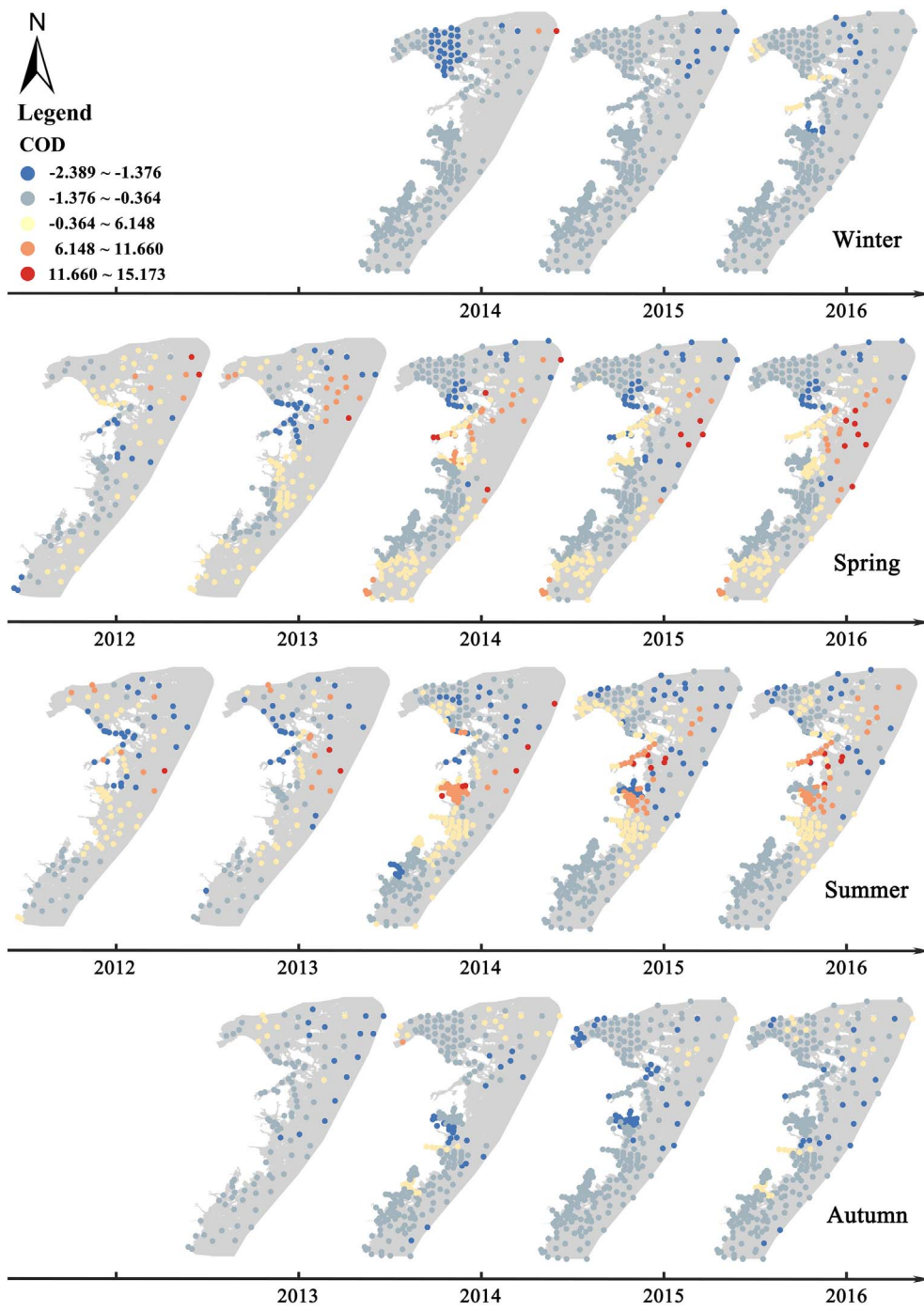


Fig. 14. Spatiotemporal distributions of parameter COD in all (totally 17) seasons from 2012 to 2016.

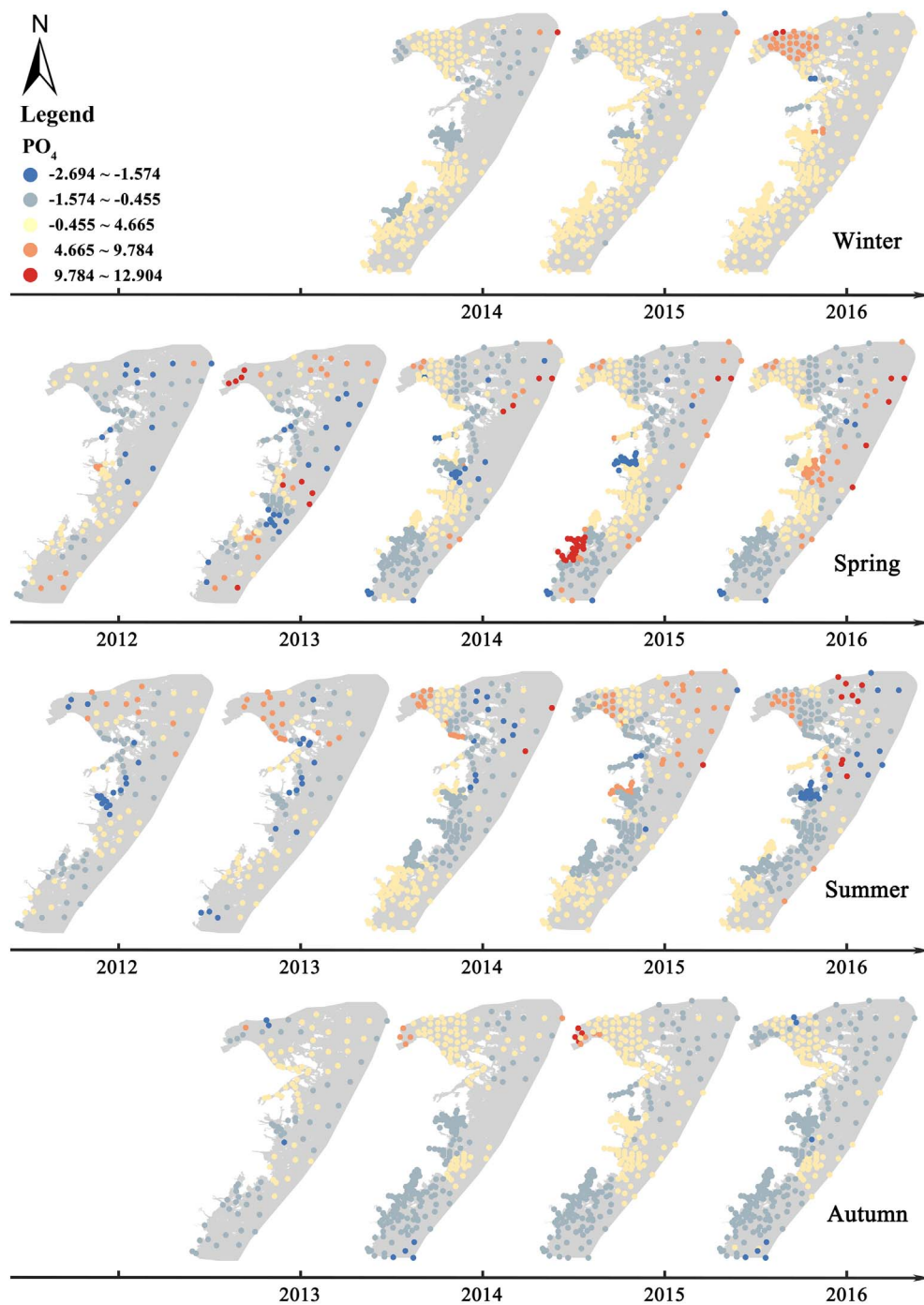


Fig. 15. Spatiotemporal distributions of parameter PO_4 in all (totally 17) seasons from 2012 to 2016.

References

Alam, R.Q., et al., 2016. Response of estuarine phytoplankton to nutrient and spatio-temporal pattern of physico-chemical water quality parameters in Little Vermilion Bay, Louisiana. *Ecol. Inform.* 32, 79–90.

Bai, Y., et al., 2016. A geographically and temporally weighted regression model for ground-level $PM_{2.5}$ estimation from satellite-derived 500 m resolution AOD. *Remote Sens.* 8, 262.

Brunsdon, C., Fotheringham, A.S., Charlton, M., 1998. Geographically weighted regression-modelling spatial non-stationarity. *J. Roy. Stat. Soc. Ser. D (Stat.)* 47, 431–443.

Brunsdon, C., Fotheringham, A.S., Charlton, M., 1999. Some notes on parametric significance tests for geographically weighted regression. *J. Reg. Sci.* 39, 497–524.

Celik, K., 2006. Spatial and seasonal variations in chlorophyll-nutrient relationships in the shallow hypertrophic Lake Manyas, Turkey. *Environ. Monit. Assess.* 117, 261–269.

Chen, J., Liu, J., 2015. The spatial and temporal changes of chlorophyll-a and suspended matter in the eastern coastal zones of China during 1997–2013. *Cont. Shelf Res.* 95, 89–98.

Chu, H., Huang, B., Lin, C., 2015. Modeling the spatio-temporal heterogeneity in the PM_{10} - $PM_{2.5}$ relationship. *Atmos. Environ.* 102, 176–182.

Cole, B.E., Harmon, D.D., 1981. Phytoplankton Productivity, Respiration, and Nutrient Uptake and Regeneration in the Potomac River, August 1977–August 1978. (Open-File Report).

Cong, M., et al., 2014. Phosphorus forms and distribution in Zhejiang coastal sediment in the East China Sea. *Int. J. Sediment. Res.* 29, 278–284.

Crespo, R., 2009. Statistical Extensions of GWR: Spatial Interpolation and A Spatiotemporal Approach. University of Ireland, Maynooth (Doctor).

Dango, E.A.S., 2015. Distribution and Seasonal Variation of Nutrient Salts and Chlorophyll-a in Surface Seawater Along Alexandria Coastal Zone Area. 3. pp. 180.

Fotheringham, A.S., Brunsdon, C., Charlton, M., 2002. Geographically Weighted Regression: The Analysis of Spatially Varying Relationships. John Wiley & Sons, UK.

Fotheringham, A.S., Crespo, R., Yao, J., 2015. Geographical and temporal weighted regression (GTWR). *Geogr. Anal.* 47, 431–452.

- Freedman, R., Sen Roy, S., 2012. Spatial patterning of *Manta birostris* in United States east coast offshore habitat. *Appl. Geogr.* 32, 652–659.
- Gollini, I., et al., 2015. GWmodel: an R package for exploring spatial heterogeneity using geographically weighted models. *J. Stat. Softw.* 63, 1–50.
- He, X., et al., 2013. Using geostationary satellite ocean color data to map the diurnal dynamics of suspended particulate matter in coastal waters. *Remote Sens. Environ.* 133, 225–239.
- Huang, B., Wu, B., Barry, M., 2010. Geographically and temporally weighted regression for modeling spatio-temporal variation in house prices. *Int. J. Geogr. Inf. Sci.* 24, 383–401.
- Keith, S.A., Kerswell, A.P., Connolly, S.R., 2013. Global diversity of marine macroalgae: environmental conditions explain less variation in the tropics. *Glob. Ecol. Biogeogr.* 23, 517–529.
- Khodse, V.B., et al., 2007. Distribution and seasonal variation of concentrations of particulate carbohydrates and uronic acids in the northern Indian Ocean. *Mar. Chem.* 103, 327–346.
- Kraak, M.J., Koussoulakou, A., 2005. A Visualization Environment for the Space-Time-Cube.
- Liu, J.P., et al., 2006. Sedimentary features of the Yangtze River-derived along-shelf clinoform deposit in the East China Sea. *Cont. Shelf Res.* 26, 2141–2156.
- Lou, X., Hu, C., 2014. Diurnal changes of a harmful algal bloom in the East China Sea: observations from GOCI. *Remote Sens. Environ.* 140, 562–572.
- Lu, B., et al., 2014. Geographically weighted regression with a non-Euclidean distance metric: a case study using hedonic house price data. *Int. J. Geogr. Inf. Sci.* 28, 660–681.
- Niu, L., et al., 2015. Statistical analysis of phytoplankton biomass in coastal waters: case study of the Wadden Sea near Lauwersoog (The Netherlands) from 2000 to 2009. *Ecol. Inform.* 30, 12–19.
- Paudel, B., et al., 2016. Spatial variability of estuarine environmental drivers and response by phytoplankton: a multivariate modeling approach. *Ecol. Inform.* 34, 1–12.
- Qiu, Z., et al., 2015. Innovative GOCI algorithm to derive turbidity in highly turbid waters: a case study in the Zhejiang coastal area. *Opt. Express* 23, 1179–1193.
- Ryan, K., Ali, K., 2016. Application of a partial least-squares regression model to retrieve chlorophyll-a concentrations in coastal waters using hyper-spectral data. *Ocean Sci. J.* 51, 209–221.
- Steingrund, P., Gaard, E., 2005. Relationship between phytoplankton production and cod production on the Faroe Shelf. *ICES J. Mar. Sci.* 62, 163–176.
- Su, Y.S., Weng, X.C., 1994. Water Masses in China Seas. *Oceanology of China Seas, China.*
- Terry, J.P., Kim, I.H., Jolivet, S., 2013. Sinuosity of tropical cyclone tracks in the South West Indian Ocean: spatio-temporal patterns and relationships with fundamental storm attributes. *Appl. Geogr.* 45, 29–40.
- Wang, Y., et al., 2015. Spatial-temporal variations of chlorophyll-a in the adjacent sea area of the Yangtze River estuary influenced by Yangtze River discharge. *Int. J. Environ. Res. Public Health* 12, 5420–5438.
- Wrenn, D.H., Sam, A.G., 2014. Geographically and temporally weighted likelihood regression: exploring the spatiotemporal determinants of land use change. *Reg. Sci. Urban Econ.* 44, 60–74.
- Wu, B., Li, R., Huang, B., 2014. A geographically and temporally weighted autoregressive model with application to housing prices. *Int. J. Geogr. Inf. Sci.* 28, 1186–1204.
- Yang, D., et al., 2013. Numerical study on the origins and the forcing mechanism of the phosphate in upwelling areas off the coast of Zhejiang province, China in summer. *J. Mar. Syst.* 123–124, 1–18.